Soft Matter

Loading causes molecular damage in fibrin fibers

Sajjad Norouzi,*[a] Matthew J. Lohr,[a] Mayar T. Ibrahim,[a] Christian M. Jennings,[a] Daniel Wang,[a] Pengyu Ren, [ID][a] Manuel K. Rausch [ID][ab] and Sapun H. Parekh [ID]*[a]

Blood clots are the body's natural biomaterials formed during wound healing, but they are also the cause of many pathologies, such as ischemic stroke. Fibrin, the main protein in clots, provides clots with mechanical strength through a network of fibrin fibers. These fibers exhibit high extensibility and primarily elastic properties under static loading conditions though little is known about single fiber mechanics under dynamic loading, as experienced *in vivo*. Indeed, many biological materials show distinct mechanical responses under repeated loading/unloading (cyclic loading), a prime example of which is clot embolization. Using lateral force microscopy, we show that fibrin fibers exhibit viscoelasticity and undergo irreversible molecular damage under cyclic loading. Cross-linking results in a more rigid structure with permanent damage occurring at larger strains – findings corroborated by computational modeling. Molecular spectroscopy analysis with broadband Raman scattering spectroscopy, combined with molecular dynamics simulations, allows identification of the damage source, unfolding pattern, and inter- and intra-molecular changes in fibrin. The results reveal partial recovery of the protein's secondary and tertiary structures, providing a deeper understanding of fibrin's molecular wear under load and its behavior in wound healing and pathologies like stroke and embolism.

Introduction

Fibrin, the pivotal protein in blood clots, plays a crucial role in wound healing and thrombosis as a scaffold that unites clot components to prevent bleeding and promote tissue repair.[1,2] The hierarchical structure of fibrin scaffolds arises from the polymerization of its precursor, fibrinogen, into fibrin fibers. Fibrinogen comprises disulfide-bonded pairs of Aα, Bβ, and γ chains.[3] Together, these chains form two distal (D-domain) and one central (E-domain) globular domains, with each D- and E-domain connected by a three-stranded, α-helical coiled-coil structure. Through the coagulation cascade, thrombin cleaves fibrinopeptide A and B from Aα and Bβ chains of fibrinogen, leaving α and β chains and creating knobs 'A' and 'B' and holes 'a' and 'b' as fibrin molecules.[3,4] These molecules grow longitudinally through knob–hole interactions, forming long 2-strand thick protofibrils that can aggregate laterally to create fibrin fibers. Protofibrils are further stabilized through the αC domain – the C-terminal part of the α chain that enhances the lateral aggregation of protofibrils.[5,6] Finally, Factor XIII (FXIII) further stabilizes the clot by forming covalent bonds in αC domain and the C-terminal part of the γ chain known as γ-nodule.[7]

Blood clots naturally experience mechanical loads in the body. They feel shear from blood flow and tensile forces from platelet contraction and muscle movements. The mechanical properties of these clots are crucial for withstanding forces, facilitating wound closure, and recommending treatment strategies for their effective removal in conditions such as thrombosis and stroke.[8] Various techniques, from atomic force microscopy (AFM) to dynamical mechanical analysis and mechanical rheology, have been employed to investigate clot mechanical features at different scales, spanning from a single fibrinogen molecule to the entire clot.[9–12] Regardless of the scale, clots or fibrin gels exhibit high extensibility and viscoelastic properties with stress-stiffening behavior; that is, an increased elastic modulus with strain.[13–16]

Single molecule spectroscopy and molecular dynamic[1] simulations have demonstrated fibrinogen's unfolding under force, starting with the unfolding in the γ-nodule and helical coiled-coil and propagating through other regions.[17] These studies show how molecular rearrangements within fibrinogen accommodate external forces. Interestingly, while the αC region shows limited contribution to the single molecule (fibrinogen) mechanical properties, this region does influence single fibrin fiber and network mechanical properties.[17–19] Cross-linking by FXIII in both αC region and γ-nodule also alters fibrin's stiffness and extensibility.[18,19] Notably, these insights have primarily relied on static (singular) loading under tension, compression, or shear, which do not exactly align with *in vivo* dynamic forces, such as

[a] *Department of Biomedical Engineering, University of Texas at Austin, Austin, TX 78712, USA. E-mail: sajjadnorouzi@utexas.edu, sparekh@utexas.edu*

[b] *Department of Aerospace Engineering and Engineering Mechanics, University of Texas at Austin, TX 78712, USA*

those applied during the respiratory cycle or muscle movements. Many biological materials exhibit different mechanical behavior under cyclic loadings compared to common acyclic scenarios.[20–22] In cyclic loadings, a material undergoes repeated loading/unloading over time, such as with peristaltic forces that occur during respiration. While techniques like AFM or optical tweezers provide insights into fiber-scale behavior,[9,23] they fall short in detailing how force propagates within the complex fibrin molecule and which parts of the molecule respond to the external force. Spectroscopic techniques, such as Fourier transform infrared (FTIR) and broadband coherent Raman anti-Stokes scattering (BCARS), offer structural information at the molecular level.[24,25] FTIR and BCARS have revealed the change in the protein secondary structure through α-helix to β-sheet transition under tension or compression, which was attributed to the unfolding of fibrin's helical coiled-coil domain. Our previous study demonstrated the involvement of the D-domain with β-sheet structures in fibrin's response to the external force,[26] consistent with β-strands unfolding in MD simulations of the fibrinogen molecule.[17] However, the role of unfolding in this domain and its interaction with the coiled-coil domain is unclear. Which domain unfolds first and to what extent? Answering this question may help clarify what parts of the molecule are responsible for the observed inconsistent increasing/decreasing trend of the α-helix to β-sheet ratio under increasing shear strain.[26] Using a combination of AFM force spectroscopy, molecular dynamics simulations, and statistical modeling, Maksudov *et al.* demonstrated that approximately 40% of peak forces in double-stranded fibrinogen oligomers are associated with mixed, simultaneous unfolding transitions.[27] These transitions depend on both the length of the oligomers and the geometry of loading.

Additionally, due to the molecular damage, the loading history may change fibrin's subsequent response to a load under cyclic loading.[20,21,28] In this work, the term "damage" refers to the process by which some bonds between different parts of the material are broken.[29] If these bonds cannot reform and the material does not return to its original condition after unloading, the damage is considered irreversible or permanent within the timescale of the experiment. While damage in fibrin has been seen before, it remains unclear whether applied forces induce permanent, molecular-level damage in fibrin and, if so, what the underlying mechanisms may be.

In this study, we employ lateral force microscopy as an application of AFM to explore the mechanical response of single fibrin fibers in different cross-linking scenarios and under cyclic loadings.[30] Subsequently, we use BCARS spectroscopy and MD simulations to elucidate fibrin's molecular behavior under cyclic loading to trace damage propagation in different molecule parts. Our observations indicate that increased cross-linking by FXIII enhances fibrin's rigidity, reducing permanent damage to fibers under tensile loading. Conversely, uncross-linked fibrin fibers show irreversible damage even at small strains, which intensifies as strain increases. BCARS data consistently depict changes in the protein's secondary and tertiary (3-dimensional (3D) conformation) structure under force for uncross-linked fibers. However, this behavior is more vivid for cross-linked fibers at larger strains.

Intermolecular interactions, particularly in cross-linked fibers, change under load, which suggests that protofibrils' lateral configuration differs before *versus* after loading. This study provides insights into fibrin's response to cyclic loading, deepening our understanding of *in vivo* blood clot behavior since the material fundamentally changes with loading history.

Materials and methods

Sample preparation

To create individual fibrin fibers for AFM experiments, fibrinogen (FIB1, Enzyme Research Laboratories) was dissolved in FB1x buffer (20 mM HEPES (BP310-100, Fisher Scientific) and 150 mM NaCl (S271-3, Fisher Scientific) at pH 7.4) to prepare a 10 mg mL^{-1} stock solution. For fluorescence imaging, unlabeled fibrinogen was mixed with Alexa 488-labeled fibrinogen (F13191, Thermo Fisher) at a 9:1 molar ratio. Fibrinogen and human alpha thrombin (HT 1002a, Enzyme Research Laboratories) were then combined with FB1x buffer containing 5 mM CaCl$_2$ (746495, Sigma Aldrich) to achieve final concentrations of 1 mg mL^{-1} fibrinogen and 0.1 U mL^{-1} thrombin. FIB1 consists of some FXIII, resulting in partially cross-linked fibrin fibers. Next, we applied 10 μL of the resulting solution onto a ridged substrate, fabricated as outlined in ref. 9. Briefly, two drops of optical adhesives (NOA 60, Norland Optical Adhesives) were cured by ultraviolet light between a mold made of polydimethylsiloxane (PDMS) (research micro stamps) with 30 μm wide trenches and ridges and a cover glass. The optically cured substrate was plasma-cleaned for hydrophilicity before pouring the fibrin gel. After incubating the fibrinogen for one hour at 37 °C in ~90% humidity, it was rinsed with FB1x buffer to remove excessive salts and weakly bound fibers. Throughout the entire experiment, the sample remained hydrated in FB1x buffer.

To inhibit the cross-linking in FIB1, we used 1,3-dimethyl-4,5-diphenyl-2-[(2-oxopropyl)thio] imidazolium, trifluorosulfonic acid salt (D004) (Zedira). D004 was dissolved in dimethyl sulfoxide (DMSO) to make a 20 mM solution, as described in ref. 31. Then, 2 μL of this solution was added (400 μM final concentration) to the fibrinogen solution before adding thrombin. We observed that 2% (v/v) DMSO did not alter the molecular structure or cross-linking of fibrin (Fig. S1).

For fully cross-linking fibrin fibers, we used exogenous Factor XIII (HFXIII 1313, Enzyme Research Laboratories), with a final concentration of 8 U mL^{-1}.[24] It was added to thrombin solution in the presence of CaCl$_2$ for full cleavage and then mixed with fibrinogen solution.

In the BCARS experiment, we created fibrin gels with higher fibrinogen and thrombin concentrations to increase Raman scattering signal (final fibrinogen and thrombin concentrations were 7 mg mL^{-1} and 1 U mL^{-1}, respectively). Indeed, fibrin gels exhibit different network properties at different fibrinogen and thrombin concentrations,[32] but we found no dependence of the Raman molecular vibrations on fibrinogen concentration (Fig. S2). The fibrin gel was formed by the fibrinogen/thrombin solution bridging two 24 mm × 60 mm plasma-cleaned

coverslips (48393-106, VWR) with a 2–3 mm gap on a manual tensile device. The gel solution was supported by a third square 22 mm × 22 mm cover glass (48366-227, VWR) coated with PEG (6–9) silane to prevent protein adhesion adapted from ref. 33. PEG coating was confirmed by incubating ATTO 488-labeled fibrinogen on the cover glass, followed by washing and fluorescence imaging. The mean fluorescence signal was significantly reduced on the PEG-coated cover glass (Fig. S3). Lateral boundaries on two coverslips were established with a hydrophobic marker. Subsequently, the gel was incubated for an hour at 37 °C with ∼90% humidity. Then, the bottom PEG-silanized cover glass was gently detached and replaced with another square cover glass spaced ∼175 μm from the gel to hold the buffer and hydrate the gel.

Lateral force microscopy

Fibrin mechanical testing was conducted using the MFP-3D atomic force microscopy (Asylum Research) equipped with inverted epifluorescence microscopy (Olympus IX 70). Optical images were acquired with a 30×, 1.05 NA silicone oil immersion objective (UPLSAPO30XS, Olympus). To ensure accurate mechanical measurements with enough resolution, soft cantilevers with nominal normal spring constants of 200 pN nm^{-1} and 20 pN nm^{-1} (PPP-LFMR, qp-SCONT, NanoAndMore) were used. All cantilevers were calibrated for lateral force microscopy (LFM) using the geometrical features and spring constant in normal mode.[34] Subsequently, when the cantilever tip is approximately in the fiber's axial plane, the cantilever is moved laterally, impinging on a single fibrin fiber and starting the pulling process.[9] The cantilever speed was set to 1 μm s^{-1}, as no differences were observed in the mechanical responses of fibrin fibers at varying loading rates (Fig. S4). In addition to recording force based on the calibrated lateral AFM signal and stage cantilever displacement, the fiber is imaged for length measurements and strain calculations. Strain is calculated as the ratio of change in fiber's length to the initial length. In LFM experiments, we neglect the local stress concentration in fibrin fibers at the point of contact with the AFM tip.

For force relaxation tests, the fiber is pulled to a certain strain (1 μm s^{-1} is the cantilever lateral velocity) and held there while recording the force until being pulled to a larger strain. In cyclic loading experiments, the fiber was pulled to a certain strain twice to differentiate viscoelastic energy dissipation and permanent damage.

Broadband coherent anti-Stokes Raman scattering (BCARS) microscopy

For molecular microscopy, we used the BCARS hyperspectral microscope that was previously used for fibrin measurements. Briefly, a laser producing sub-100 picosecond pulses at 1 MHz repetition rate at 1064 nm and a broadband supercontinuum with a spectrum ranging from 1100 nm to 2400 nm (Leukos Opera HP, Leukos) was used for excitation. The two beams were focused by a 100×, 0.85 NA objective (LCPLN100XIR, Olympus). The signal was collected in transmission by a 20×, 0.4 NA objective (M-20X, MKS Newport).

The formed fibrin gel on the tensiometer was mounted on the BCARS stage. The gel was fixed at one end while the other end could move by a manual micrometer. The uniaxial tension was applied by turning the micrometer, and the strain was calculated based on the ratio of deformation to the initial gauge length. In the cyclic loading, the gel was pulled to each strain twice and then returned to the relaxed state. The pixel size was chosen 1 μm × 1 μm, and the CCD integration time for each spectrum was ∼200 ms to maximize the signal while avoiding saturation. The experiment was conducted for both uncross-linked and partially cross-linked (without inhibiting or adding cross-linkers to FIB1) fibrin gels with four and five replicas, respectively.

BCARS signal processing

BCARS raw signals were converted into Raman spectra based on the methodology outlined in literature.[4,5] BCARS spectra with an average spectral resolution of 4 cm^{-1} was recorded over a range of 700 cm^{-1} to 4000 cm^{-1} Raman shift. After phase retrieval, all the spectra were normalized based on the total Amid I area (1600 cm^{-1} to 1700 cm^{-1}), showing the protein secondary structure. Subsequently, the background was subtracted from each spectrum based on the intensity at the smallest Raman shift. Each spectrum was at least the average of 3 × 3 pixels. For molecular analysis, the ratio of α-helix (mean intensity in the range of 1645 cm^{-1} to 1655 cm^{-1}) to β-sheet (mean intensity in the range of 1669 cm^{-1} to 1679 cm^{-1}),[35] the intensity at 3065 cm^{-1} (mean intensity in the range of 3060 cm^{-1} to 3070 cm^{-1}) as the indication of aromatic amino acids,[36] and the intensity at 2934 cm^{-1} (the mean intensity in the range of 2929 cm^{-1} to 2939 cm^{-1}) as CH$_3$ symmetric vibrations[35] were plotted for each strain in violin plots.[37] Statistical analyses were done based on non-parametric Wilcoxon signed-rank test.

Computational modeling of cyclic loading

We developed a computational model to capture the visco-hyperelastic and damage properties of the fibrin fibers under cyclic loading. Specifically, we fit a quasi-linear visco-hyperelastic damage model to data on force, time, and displacement from the cyclic loading tests using custom MATLAB scripts. We modeled fiber deformation as a combination of two uniaxial extension problems and assumed that its deformation was isochoric. Note that, because we did not have accurate measures of diameter, we used a diameter of 150 nm for all samples. This was chosen as it is within the diameters reported for individual fibrin fibers by Belcher et al.[38] Using this fixed value allowed us to compare the parameters across samples; however, it did not allow us to make accurate comparisons of the fibers' stiffnesses. Also, note that we do not include the bending of the fiber in our model; this is because the bending does not contribute significant energy to the system at the strains in these mechanical tests. Our SI contains a figure showing the distribution of energies between bending and stretching (Fig. S5). Using the initial position of the AFM cantilever along the fiber and its horizontal and vertical displacements, we calculated the stretch that the fiber would feel due to the moving beam. To model the visco-hyperelastic properties of the fibers, we implemented a quasilinear viscoelastic model from

Simo and Hughes.[39] In this model, the principal components of the visco-hyperelastic stress take the form

$$S_a = \int_{\infty}^{t} g(t-s) \frac{d}{ds}\left[\text{Dev}\left(\frac{1}{\lambda_a}\frac{\partial W^o(\lambda_a(s))}{\partial \lambda_a}\right)\right] ds. \quad (1)$$

Here, a indexes the principal coordinate axes and $\text{Dev}(\bullet) = [\bullet] - \frac{1}{3}[\bullet:\mathbf{C}]\mathbf{C}^{-1}$. Here, $\mathbf{C}$ is the right Cauchy–Green tensor and is defined as $\mathbf{C} = \text{diag}(\lambda_1^2, \lambda_2^2, \lambda_3^2)$. Note that boldface denotes that a given variable is a second-order tensor. For our hyperelastic strain energy function, W^o, we used a one-term Ogden model, which is an isotropic model defined as

$$W^o(\lambda_1, \lambda_2, \lambda_3) = \frac{2\mu}{\alpha^2}\left[\lambda_1^\alpha + \lambda_2^\alpha + \lambda_3^\alpha - 3\right]. \quad (2)$$

The Ogden model uses the principal stretches, λ_i ($i = 1, 2, 3$), of the deformation. Because we did not have equipment capable of measuring the volume change of the fiber, we assumed that there was no volume change. Thus, we excluded the volumetric portion of the stress from eqn (1). Due to our incompressibility assumption, the stretches of our uniaxial loading are found to be $\lambda_1 = \lambda$ and $\lambda_2 = \lambda_3 = \frac{1}{\sqrt{\lambda}}$. Here, λ is the stretch in the direction of the loading, x_1. The parameter α governs the strain-stiffening behavior of the material and μ is the shear modulus of the material. Note that W^o is the isochoric portion of the strain energy.

We used a two-term ($N = 2$) Prony series for our normalized relaxation function, $g(t)$. This modulus, which captures the time-dependent behavior of the fiber, is defined as

$$g(t) = \gamma_\infty + \sum_{i=1}^{N} \gamma_i. \quad (3)$$

Here, $\tau_i > 0$ are the relaxation time constants and $\gamma_i \in [0, 1]$ are moduli subject to the following constraint

$$\sum_{i=1}^{N} \gamma_i = 1 - \gamma_\infty. \quad (4)$$

Here, γ_∞ is the long-term modulus corresponding to a fully relaxed material.

We model the progressive, Mullins-like damage of fibrin fibers through the Simo damage model.[40] In this model, the damage is a function of the maximum stretch a body has experienced in its loading history. The body only undergoes damage when it is stretched beyond its previous maximum stretch. To this end, our effective stress, $\bar{\mathbf{S}}$, is defined as

$$\bar{\mathbf{S}} = D(W^o)\mathbf{S}, \quad (5)$$

where $D(W^o) \in [0, 1]$ is a damage function with the form

$$D(W^o) = d_1 + [1 - d_1]\frac{1 - \exp\left(-\frac{\Xi}{d_2}\right)}{\frac{\Xi}{d_2}}. \quad (6)$$

Here, $d_1 \in [0, 1]$ and $d_2 > 0$ are parameters governing the damage evolution, and Ξ is defined as

$$\Xi = \max_{s\in(-\infty,t)} \sqrt{2W^o(\lambda(s))}. \quad (7)$$

Note that this damage formula captures the Mullins-like effect seen in repeated loading of fibrin fibers.[41] We implemented the integration algorithm for nonlinear viscoelasticity from Simo and Hughes[39] to calculate S_a in eqn (1). Also, note that we fit the model to the lateral force using data on force, time, and displacement. Our error function for this optimization process was

$$\text{error} = \frac{F^{exp} - F^{num}}{\max(F^{exp})}, \quad (8)$$

where F^{exp} is the force measured in the experiment, and F^{num} is the force computed by the numerical model. We minimized the total error using a nonlinear least squares solver with the trust-region-reflective algorithm within MATLAB. Note that we fit all model parameters (μ, α, γ_i, τ_i, d_1, d_2) at once.

Molecular dynamics simulations of single molecule fibrinogen stretching

The crystal structure of a single fibrinogen molecule (PDB ID: 3GHG)[42] was obtained from the Protein Data Bank, which differs from the first resolved crystal structure of the bovine fibrinogen molecule.[43] Although the full-length fibrinogen consists of three chains (Aα, Bβ, and γ), the available crystal structure lacks the C-terminal regions of all three chains as well as the majority of the highly flexible and intrinsically disordered αC domain of the Aα chain. These missing regions were not reconstructed since the αC domain does not play a direct role in axial tensile strength or structural resistance of a single molecule pulling.[5,44] System preparation was conducted using the GROMACS package[45,46] with the CHARMM27 force field.[47] The default protocol was followed, including solvation in a water box (cutoff: 10.0 Å) using the TIP3 water model, and neutralization to physiological salt concentration by adding Na$^+$ ions. The system was then energy-minimized and equilibrated under canonical ensemble with constant number of particles, volume, and temperature (NVT) and isothermal–isobaric ensemble with constant number of particles, pressure, and temperature (NPT) conditions. Next, the equilibrated system was subjected to two independent pulling simulations using CustomBondForce in OpenMM 8 package.[48] The pulling force was applied to ILE394 in γ-nodule 1 at one end of the fibrinogen molecule, while GLY395 in γ-nodule 2 at the other end of the protein remained fixed. The pulling simulations were conducted using a harmonic potential, in which the applied force is proportional to the deviation from a reference separation between ILE394 and GLY395. This setup enables the pulling rate to emerge naturally from the system's internal dynamics, rather than being enforced externally. As a result, the system evolves under quasi-equilibrium conditions, with strain accumulating through thermal fluctuations around the spring's equilibrium point, rather than through a constant imposed velocity (Fig. S6 for rate distributions). To achieve the corresponding experimental strain of 16.67%, a pulling force

constant of 1000.0 kJ mol^{-1} nm^{-1} was applied (Pull 1, Fig. S7), followed by an 8 ns relaxation phase (Relax 1, Fig. S7) without external force to reach the lowest possible strain. For the second pulling simulation (Pull 2, Fig. S7), a lower force constant of 50 kJ mol^{-1} nm^{-1} was used to achieve the same strain, followed by a 5 ns relaxation phase (Relax 2, Fig. S7). The strain was calculated as the ratio of the molecule extension to the fibrinogen initial length between two ends of the protein (ILE394 & GLY395).

During the initial pulling simulation (Pull 1), the target strain of 16.67% was reached within 200 ps and remained stable for the remainder of the 1 ns pulling time (Fig. S7). The final frames from two independent Pull 1 replicas were selected as representative structures (Fig. S7) and used as the starting state for the subsequent Relax 1 phase. Relax 1 was run for 8 ns, but after 6 ns, strain spikes were observed in both replicas (Fig. S7). Therefore, the final frame at 6 ns was chosen as the representative structure for Relax 1 and used as the seed structure for the next pulling simulations. For the second pulling simulation (Pull 2), a lower pulling force constant ($k = 50.0$ kJ mol^{-1} nm^{-1}) was applied. The 16.67% strain was achieved at 400 ps for Replica 1 and 800 ps for Replica 2, with stable strain values reflecting structural stability (Fig. S7). The final frames were selected as representative structures. These selected structures from Pull 2 were used to initiate the Relax 2 phase, which was run for 5 ns in two independent replicas. The last frames of these simulations were chosen as representative structures for this phase.

Ramchandran plots were generated using MDAnalysis2.9.0.[49,50] The α-helix/β-sheet ratio was determined based on the number of points within the areas assigned to each secondary structure. α-Helices were identified within φ angles ranging from $-120°$ to $-30°$ and $60°$ to $90°$, while ψ angles ranged from $-60°$ to $-30°$ and $0°$ to $60°$. β-Sheets were also characterized by φ angles between $-180°$ and $-45°$ and ψ angles from $60°$ to $180°$.[51] The ranges of α-helix and β-sheet angles are chosen based on the two primary allowed regions of α-helices and the one allowed region of β-sheets.[52]

Results

Single fibrin fiber mechanics show stress relaxation

Using the AFM for LFM, we deformed single fibrin fibers inspired by work by Guthold and colleagues.[9,30] We initially conducted force relaxation experiments for single fibrin fibers that are: uncross-linked, partially cross-linked, and fully cross-linked by FXIII. Single fibers were pulled to a specific strain and held at that strain while recording the force signal. The force signals at different strain steps for three different fibers are shown in Fig. 1A–C, with the force recorded on the left axis and the corresponding strain steps on the right axis. Notably, as the strain increases, fibrin fibers, independent of the cross-linking state, relax more. In cases where the material is purely elastic, there is no stress relaxation, and the force remains constant, as observed in the fibrin fibers subjected to very small strains. To assess and compare the effect of cross-linking on viscoelastic properties, we calculated the mean square error (MSE) for the force response at each strain step. The MSE value is the
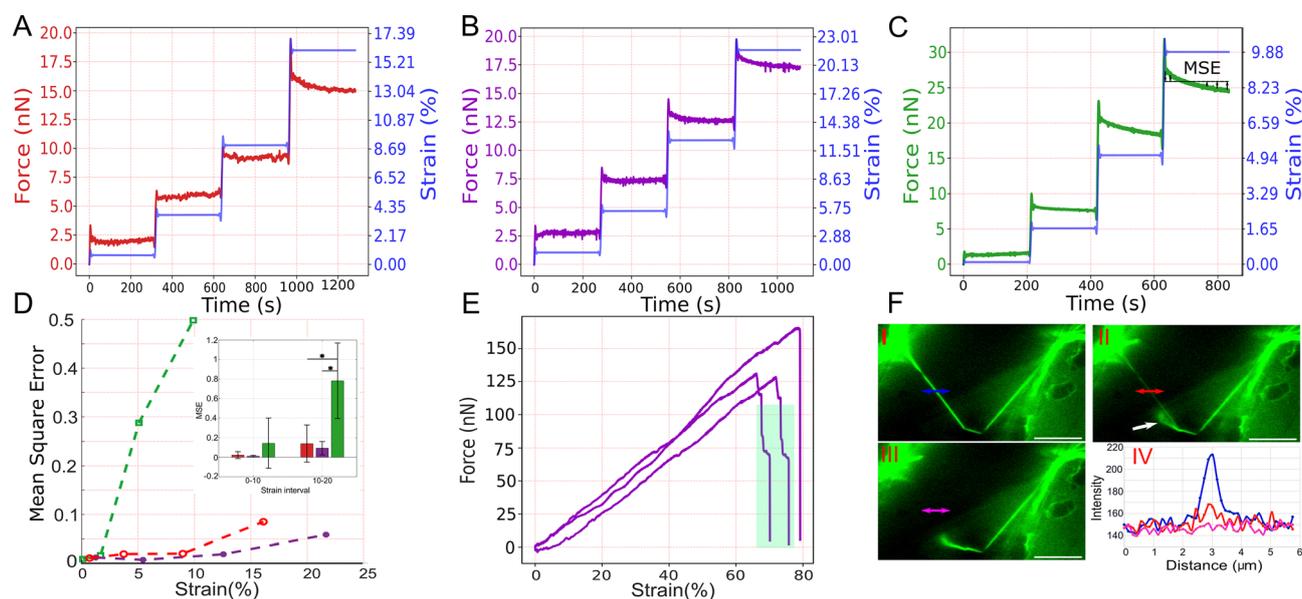
Fig. 1 Relaxation tests for fully cross-linked (A), partially cross-linked (B), and uncross-liked (C) fibrin fibers. (D) Mean square error (MSE) of the force in each strain step for the three groups shown in (A)–(C), indicating the deviation of the relaxation curve from the mean force value. The inset highlights the MSE for strains of 0–10% and 10–20%. Red, purple, and green represent fully cross-linked, partially cross-linked, and uncross-linked fibers, respectively, with sample sizes of 6, 6, and 5 fibers across 2, 2, and 3 replicates. Error bars represent standard deviation, and asterisks (*) indicate $p < 0.05$. (E) Force–strain curve for three different partially cross-linked fibrin fibers. The shaded area shows the region where catastrophic breakage of fibers often occurred. (F) The fraying pattern of a fully cross-linked single fibrin fiber at the breakage point. I to III are three consecutive snapshots of fiber rupture. The 2-sided arrows' intensity is plotted in IV and the white arrow shows the frayed fiber. The scale bar is 10 μm.

deviation of the data from the mean force value, a representative constant force, as would be the case for fully elastic materials. Fig. 1D shows the MSE for different fibers in Fig. 1A–C at varying strains, highlighting how uncross-linked fibers deviate from the mean value (the ideal elastic response) even at very small strains (5% strain). The inset shows the MSE for several fibers with different cross-linking scenarios across strain ranges, demonstrating that uncross-linked fibers exhibit larger MSE than cross-linked fibers. Cross-linking results in more elastic fibers, delaying energy dissipation until larger strains are reached. Also, we note that the calculated forces are higher for uncross-linked fibers than for cross-linked ones in Fig. 1A–C. We attribute this trend to potential differences in fiber geometry. Although fibrinogen and thrombin concentrations were identical, the resulting fiber diameters may exhibit a broad distribution. Liu *et al.* reported fiber diameters ranging from 124–800 nm for cross-linked and 94–708 nm for uncross-linked fibers.[9] When combined with the reported elastic moduli for cross-linked and uncross-linked fibers, which vary with diameter, it is possible that uncross-linked fibers can, under certain conditions, sustain larger forces than cross-linked fibers. This is further supported by the cross-sectional line profile of the fluorescent intensity from the uncross-linked fiber in Fig. 1 showing a greater width compared to the fully cross-linked fiber (Fig. S8). In Fig. 1E, the force–strain response of three partially cross-linked fibrin fibers is presented until rupture. Notably, instead of stress, we plot force, considering the small scale of fibrin fibers, where the continuum mechanics

assumption of a uniform rod can be inappropriate. Previous work showing that, as fiber diameter increases, fiber's elastic modulus decreases,[9,53,54] supports the idea that fibrin fibers may not be uniform rods. Thus, calculating stress by normalizing force with the fiber cross-sectional area may not properly account for the size-dependent heterogeneous properties in each cross-section. The highlighted region in Fig. 1E shows the force dropping in two or three steps before full rupture. Fig. 1F(I) and (II) provides two consecutive snapshots of a fully cross-linked fibrin fiber just before rupture in Fig. 1F(III). The intensity of the image through a cross-section is plotted in Fig. 1F(IV), demonstrating a reduction in the fiber's cross-section intensity before complete rupture. This stepwise drop in force and decrease in fiber intensity indicate that fibers fray before experiencing full breakage. This phenomenon is further illustrated in frayed fiber in Fig. 1F-II (white arrow).

Cyclic loading reveals permanent damage in fibrin fibers

Motivated by the dynamic nature of *in vivo* conditions, we next conducted cyclic loading experiments on single fibrin fibers. Fig. 2 illustrates the force–strain response of both uncross-linked and partially cross-linked fibrin fibers under cyclic loading. In this experiment, each fiber was pulled to a certain strain during loading and then released during unloading. We performed two loading cycles to discern material damage *versus* viscoelastic energy dissipation under the assumption that most damage would occur during the initial loading. The loading–unloading cycles were performed sequentially, with no resting
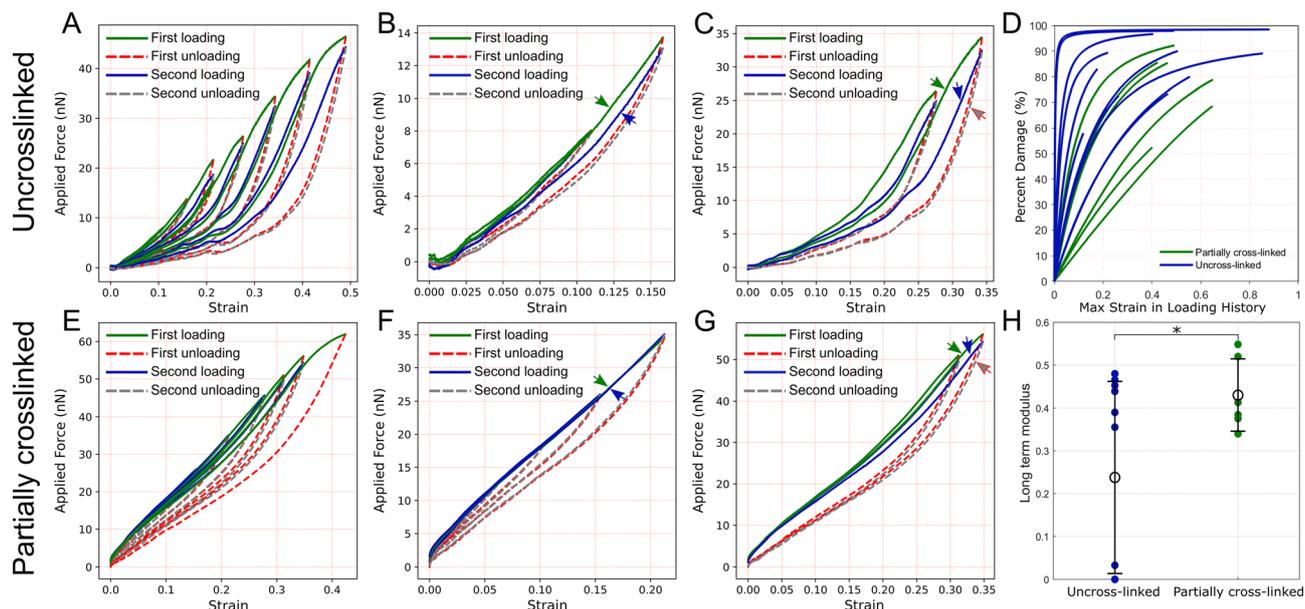
Fig. 2 Force–strain response of single fibrin fibers in cyclic loadings. (A) The uncross-linked force–strain response in cyclic loadings. The fiber is pulled twice to each strain, named as the first and second loading/unloading. (B) The cyclic response of uncross-linked fibers in small strain (<0.20). (C) The force–strain response of the uncross-linked fiber in large strain (<0.35). Green, blue, and red/grey arrows point out to the first loading, second loading, and first/second unloading, respectively. (D) Uncross-linked fibers, shown in blue, undergo damage to a greater degree and more rapidly than partially cross-linked fibers, shown in green. (E) The force–strain response of partially cross-linked fiber in a cyclic loading. The fiber is stretched twice to each strain, named as the first and second loading/unloading. (F) The cyclic response of the fiber in (E) in small strain (<0.25). (G) The force–strain curves of the fiber in (E) in large strain (<0.35). (H) Uncross-linked fibers have a smaller long-term modulus (γ_∞) than partially cross-linked fibers (11 uncross-linked fibers across 4 replicates, and 6 partially cross-linked fibers from 4 replicates). This long-term modulus is a normalized, unitless quantity.

period between cycles, to mimic physiological conditions in which clots are continuously subjected to load. In one trial, we applied two consecutive loading cycles, while the third cycle was performed after a 15-minute recovery period. As illustrated in Fig. S8, no recovery was observed after longer resting time; the third cycle still showed clear evidence of damage. In Fig. 2, the applied forces remained below 100 nN (the rupture forces for uncross-linked and cross-linked fibers are 233 nN and 581 nN, respectively[19]). This force range can be encountered *in vivo*. For example, individual platelets are capable of exerting forces in the range of 1–100 nN on fibrin fibers. For reference, a force of 4 nN is estimated to stretch an 80 nm-long fibrin fiber by 64 nm (80% strain).[55] Other factors, such as muscle movement, can also generate forces that suffice to rupture blood clots in wounds. In this study, in addition to examining larger strains associated with higher forces, we investigated whether lower forces corresponding to small strains can also induce molecular damage in fibrin.

Fig. 2A presents consecutive cyclic experiments for an uncross-linked fiber with increasing strain. The fiber exhibits only viscoelastic behavior at very small strains as the first and the second loadings coincide while the first loading and first unloading differ. However, permanent changes become apparent as the first and second loadings deviate from one another at ∼15% strain, illustrated in Fig. 2B. At larger strains, shown in Fig. 2C, the deviation between the first and second loadings becomes more pronounced, indicating more prominent damage. Interestingly, the second loading follows a different path between the first loading and the first unloading, indicating that a combination of viscoelasticity and damage occurs (discussed further in the Discussion).

Fig. 2E depicts a similar cyclic experiment for a partially cross-linked fibrin fiber. In small strains, the first and second loading curves overlap, indicating that cross-linked fibers exhibit only viscoelasticity with no noticeable damage in small strains (up to ∼20% strain, Fig. 2F). However, as the strain increases, the second loading again takes a different path between the first loading and unloading, suggesting permanent changes in fiber's structure (Fig. 2G). Generally, the degree of cross-linking correlates with mechanical reversibility (the degree to which the material can recover its initial mechanical state in cyclic loadings) in fibrin fibers. As the fibrin fibers become more cross-linked, they show permanent damage in larger strains.

Fig. 2D shows the evolution of damage calculated with a computational model of fiber deformation throughout the first loading cycle. In this figure, we plot $[1 - D(W^o)] \times 100\%$ for ease of interpretation. The damage function, $D(W^o)$, scales down the stiffness of the fibers. In this figure, the percent damage represents the percent degradation of the original stiffness of the fiber. Uncross-linked fibers experience damage much more rapidly and to a higher degree than partially cross-linked fibers.

Fig. 2H shows the long-term moduli calculated for all samples using the computational model. There is a significant difference between partially cross-linked and uncross-linked fibers. To perform this statistical analysis, we used Welch's *t*-test in R. This modulus reflects the percentage of the material

response that is purely elastic. Here, the mechanical response of partially cross-linked fibers has a larger elastic portion than uncross-linked fibers, consistent with experimental data.

Exemplary fits to the partially cross-linked and uncross-linked fibers are shown in the SI (Fig. S10 and S11). Furthermore, the parameters identified with our computational model are given for each fit (Tables S1 and S2). Interestingly, both relaxation time constants for partially cross-linked fibers are of order seconds. This is counter to the relaxation time constants for the uncross-linked fibers, where the two relaxation time constants have different orders of magnitude (Fig. S12). For these uncross-linked fibers, one modulus is on the order of seconds and the other is of order minutes. This means that partially cross-linked fibers could be modeled using a one-term ($N = 1$) Prony series, while the uncross-linked fibers need a two-term ($N = 2$) Prony series. Additionally, while the strain stiffening parameter, α, is higher in partially cross-linked fibers, it is not statistically significant (Fig. S13).

BCARS molecular microscopy reveals the origins of molecular damage

To further probe changes in fibrin during loading with molecular insights, we used BCARS spectral imaging on fibrin gels that were cyclically loaded. As a vibrational spectroscopy technique, BCARS can reveal how different molecular modes are locally modified under different loading conditions.[24,26] In each experiment, we cyclically deformed fibrin gels: initially pulled to ∼16% strain, then released to the original relaxed (0% strain) state, and this process was repeated a second time. Subsequently, the same gel was cyclically deformed to ∼66% strain (large strain) in a similar way. At each strain state, BCARS hyperspectral data were collected. BCARS imaging started when the gel exhibited no visible creep under the microscope.

Fig. 3A and D show the mean spectrum of each state for uncross-linked and partially cross-linked fibers, respectively, normalized based on the area under the curve in the Amide I region (1600 cm^{-1} to 1700 cm^{-1}). Amide I region contains information about protein secondary structures, including α-helices at 1649 cm^{-1} and β-sheets at 1672 cm^{-1}.[56] The ratio of α-helix mean intensity over the range of 1645 cm^{-1} to 1655 cm^{-1} to β-sheet mean intensity in the range of 1669 cm^{-1} to 1679 cm^{-1} is plotted in Fig. 3B and E for uncross-linked and partially cross-linked fibrin gel, respectively. For uncross-linked fibers (Fig. 3B), the median of the α-helix to β-sheet ratio increases in the first small strain, followed by a further increase in the second loading. In the relaxed states (Relax1 and Relax2), the secondary structure exhibits partial reversibility even in small strains, as the ratios are reduced relative to the strained states but not entirely to the initial state. Interestingly, at large strain, compared to ratio in the previous Relax state, the ratio did not change under 66% strain. Fig. 3C and F show the intensity at 3065 cm^{-1}, assigned to aromatic amino acids. The amplitude of this vibration serves as an indication of water–protein interactions under force.[36] For uncross-linked fibrin gels (Fig. 3C), there is no significant difference in this aromatic mode between loading and relaxation states at small strains. However, the median intensity in
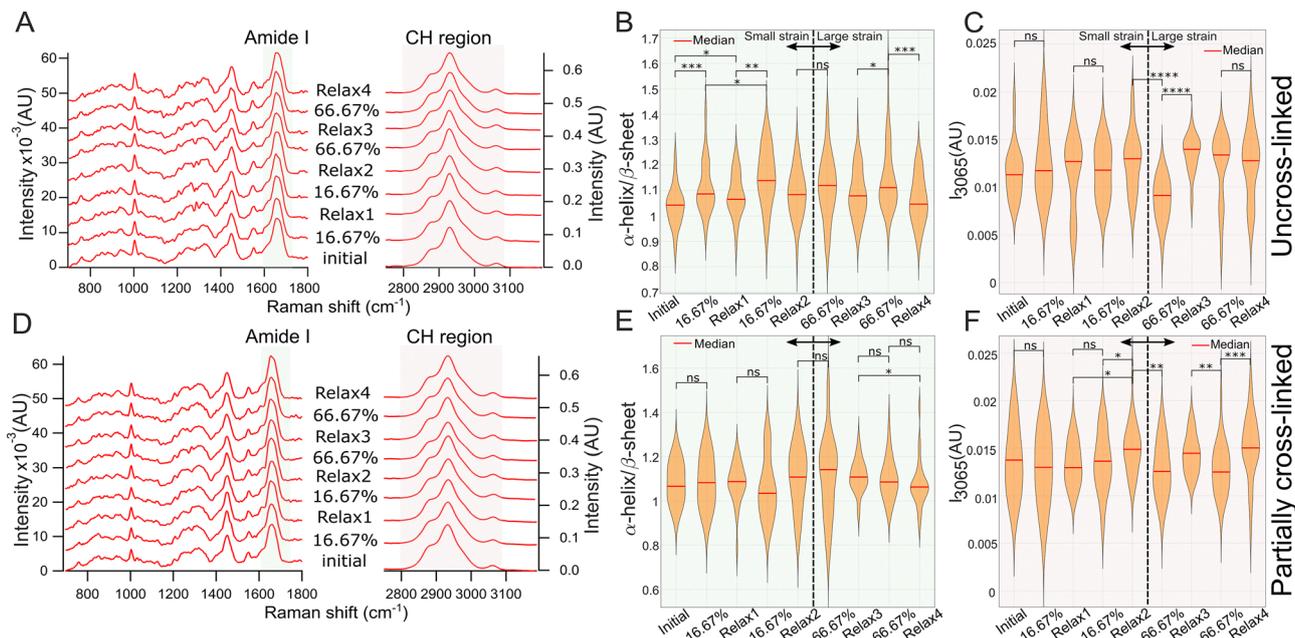
Fig. 3 BCARS molecular spectroscopy on fibrin gel under cyclic loadings. (A) Mean BCARS spectra for uncross-linked fibrin gel in different states, normalized based on area under the curve in Amide I. (B) α-Helix mean intensity over β-sheet mean intensity in different states for uncross-linked fibrin fibers. (C) Aromatic amino acid mean intensity at 3065 cm^{-1} for different states for uncross-linked fibers. (D) Mean BCARS spectra for partially cross-linked fibrin gel in different states, normalized based on area under the curve in Amide I. (E) and (F) α-Helix mean intensity over β-sheet mean intensity and intensity at 3065 cm^{-1} in different states of cyclic loading for partially cross-linked fibrin gel. 16.67% and 66.67% refer to the amount of strain. *, **, ***, **** show p-value smaller than 0.05, 0.01, 0.001, and 0.0001, respectively, and ns means "no significant difference." Each state has about 30 data points from 4 and 5 experiments for uncross-linked and partially cross-linked fibrin gels, respectively.

Relax1 is larger than the initial state and appears recoverable after the second loading in Relax2. At large strains, the first pull significantly reduces the 3065 cm^{-1} intensity. This intensity does not return to the same value in the second pull, signifying total, irreversible damage with this initial large deformation.

For partially cross-linked fibers (Fig. 3E and F), generally smaller and less significant changes are observed at small strains compared to uncross-linked fibers. As shown in Fig. 3E, the α-helix to β-sheet ratio remains almost unchanged at small strain. For cross-linked fibrin at large strain, we expected to observe more α-helix to β-sheet transition under force;[26] however, the median ratio remains unchanged in the first loading to 66% strain and then returns at Relax3 to almost the same value as in Relax2. Then, a statistically significant change is observed in Relax4, as shown by the lower value compared to Relax3, indicative of accumulated damage. Moving to the aromatic intensity at 3065 cm^{-1} in partially cross-linked networks (Fig. 3F), we observe that the vibration does not follow the same trend observed for uncross-linked fibers. However, the values at Relax1 and 2 are significantly different, indicating irreversible changes in the conformation of the protein, even in small strains. At larger strains, consistent with uncross-linked fibers, the aromatic amino acids' intensity decreases in both the first and second loadings compared to the immediately preceding Relax state, with approximate reversibility observed in Relax3 and 4. The spectroscopic results from aromatic amino acids are consistent with changes in the CH$_3$ intensity at 2934 cm^{-1} for different strain levels (Fig. S14A and B), highlighting irreversible damage

in fibrin's tertiary structure, predominantly in uncross-linked fibers. Additionally, consistent with the results from the AFM experiments, compared to partially cross-linked fibers, large strains cause more damage (irreversible Raman intensity) to uncross-linked fibers.

Unfolding of secondary structures reflects irreversible damage in uncross-linked fibrinogen

Different domains of a single fibrinogen molecule are shown in Fig. 4A. A qualitative assessment of the representative structures across different pulling and relaxation states shows substantial configurational changes in γ-nodule 1 (Fig. 4B), while coiled-coil regions exhibit more subtle changes (Fig. 4C and D). In Pull 1, unfolding begins near ILE394, the pulling point in γ-nodule 1. Several secondary structure elements are completely disrupted, including: α-helices: Phe389–Thr393, Ala289–Asp291, Lys356–Ser358 and β-sheet: Lys380–Pro387. Additionally, β-sheet Ala279–Gly284 partially unfolds, splitting into two smaller β-sheets (Phe265–Val267 and Leu276–Tyr280). In Relax 1, β-sheet Ala279–Gly284 completely unfolds, while α-helix Lys356–Ser358 recovers its structure. This suggests that α-helices are more likely to recover upon relaxation. During Pull 2, α-helix Ala289–Asp291 recovers, while α-helix Lys356–Ser358 unfolds again and β-sheet Gly188–Arg197 also begins to unfold. In Relax 2, β-sheet Gly188–Arg197 recovers, while α-helix Ala289–Asp291 remains unfolded. These features in Relax 1 and Relax 2 that do not return to their original configuration represent irreversible damage.
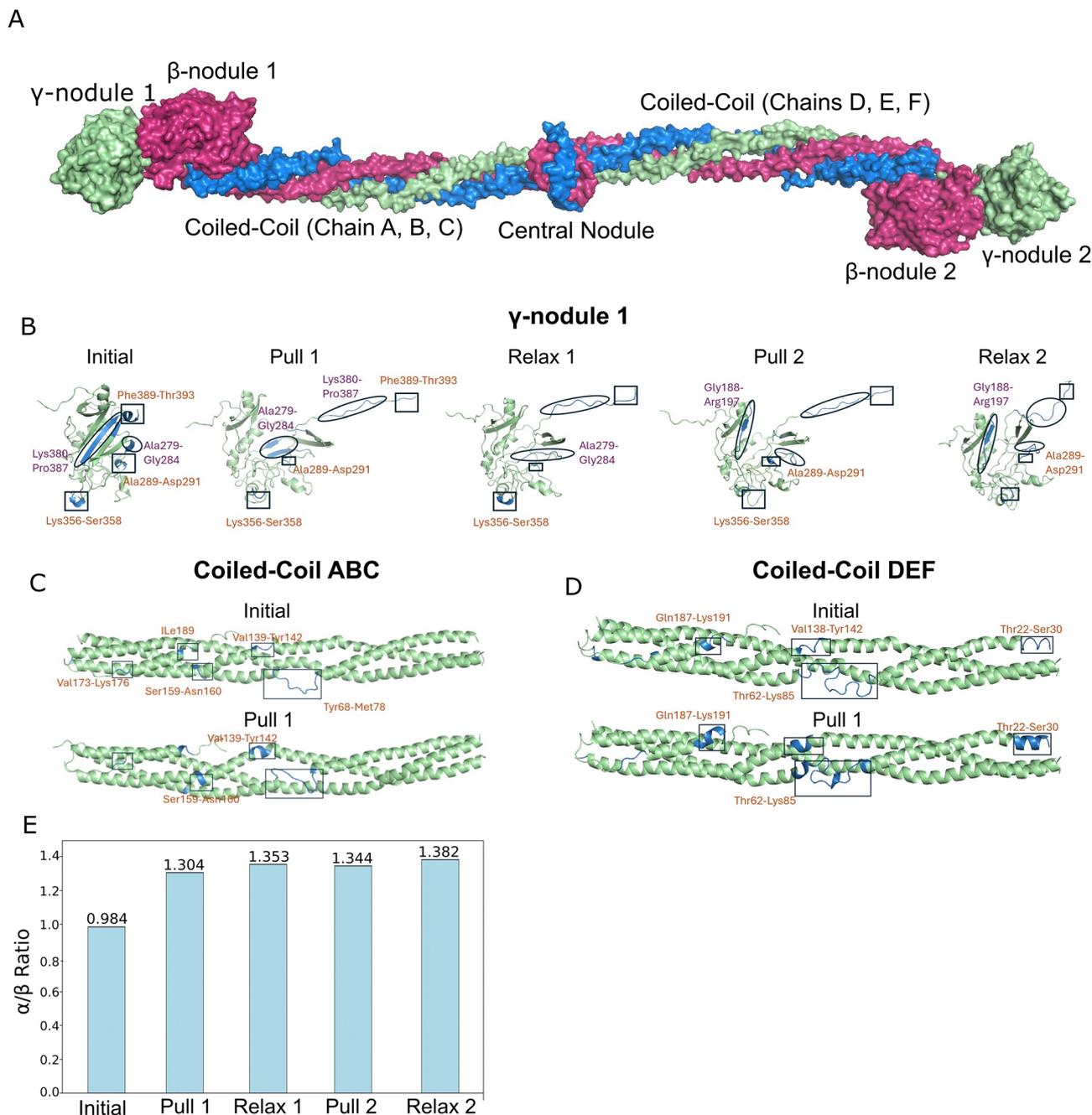
Fig. 4 MD simulation of cyclic loading on a single fibrinogen molecule. (A) The different domains of the protein: γ-nodules 1 & 2, β-nodules 1 & 2, central nodule, coiled-coil ABC, and coiled-coil DEF; (B) observed changes in γ-nodule 1 based on the selected structures representative of the experimental strain percent, changes in β-sheets represented by circle and labeled in purple, changes in α-helix represented by square and labeled in orange. Only the regions that undergo structural changes are labeled at each phase; (C) observed changes in the coiled-coil structures ABC and (D) DEF, changes in loops are represented by squares and labeled in orange (E) α-helix/β-sheet ratio of the whole fibrinogen protein throughout cyclic loading.

Additionally, the coiled-coil structures (Fig. 4C and D) exhibit significant loop rearrangements throughout cyclic pulling and relaxation. During Pull 1, the following changes are observed in coiled-coil ABC: complete folding of loop Thr22–Ser30 and loop Val138–Tyr142, partial folding of loop Thr62–Lys85, and slight folding in the terminal loop adjacent to α-helix Gln187–Lys191. In Relax 1, the loop adjacent to α-helix Gln187–Lys191 unfolds and loop Thr62–Tyr142 forms a longer

α-helix compared to Pull 1 (Fig. S15). Surprisingly, during Pull 2, more folding occurs in the loop adjacent to the α-helix at residue Glu172, followed by more unfolding in Relax2.

The coiled-coil DEF region follows a similar trend to coiled-coil ABC, as shown in Fig. 4D. Several loops in coiled-coil DEF fold in Pull 1 including: loop Val139–Tyr142, similar to coiled-coil ABC, loop Ser159–Asn160, loop at ILE189, loop Val173–Lys176, and terminal loop Tyr68–Lys78. In Relax 1, no

significant structural changes are observed. During Pull 2, the region Val173–Lys176 near the helix undergoes further unfolding, followed by the loop Ser159–Asn160 regaining its original structure in Relax 2 (Fig. S16).

The α-helix/β-sheet ratio of the fibrinogen molecule changes in response to different loading and unloading phases (Fig. 4E). The ratio increases in both Pull 1 and Pull 2, aligning with experimental data (Fig. 3B). However, during the Relax 1 and Relax 2 phases, a higher α-helix/β-sheet ratio is observed, different from experimental results. This discrepancy may be attributed to the retained strain in the relaxed structures within 6 ns of relaxation. Unlike in AFM experiments, a 0% strain state was not achieved in computational simulations.

Discussion

Cross-linking changes force propagation through fibrin fibers

Fibrin fibers display exceptional properties like high extensibility and non-linear viscoelastic behavior.[30,57] Their hierarchical structure comprises aggregated, long protofibrils formed through knob–hole interactions between fibrin molecules. When force is initially applied to fibrin fibers, potentially twisted protofibrils align with the force's direction, stretching the γ–γ cross-links between protofibrils and the αC domain—an integral component involved in lateral assembly.[19,57] At larger strains, the fibrin molecule experiences increased force, leading to the unfolding of the helical coiled-coil and γ-nodule in the D-domain, as demonstrated by single molecule force spectroscopy and MD simulations.[17] FXIII makes fibrin fibers more rigid as it cross-links both the αC domain and γ-nodule, increasing fibrin's stiffness.[18,19] The participation of cross-linking in fibrin's response to external force results in a more solid behavior with less energy dissipation shown by our AFM experiments, as expected. Non-covalent bonds, such as hydrogen bonding, are considered sources of energy dissipation in polymers, leading to more viscoelastic behavior.[58,59] The effect of cross-linking is also evident in small strains. Uncross-linked fibers exhibit viscoelastic behavior from small tensile strains where protofibrils align, and the unstructured αC domain is engaged as an entropic spring. Conversely, cross-linked fibrin fibers show increased elasticity and less dissipation. The decreased dissipation, particularly at small strains, underscores the presence of cross-linkers in the αC domain. Finally, independent of cross-linking, fibrin fibers underwent fraying before the final rupture, observed in both mechanical responses and fluorescence imaging. This suggests that lateral interactions between protofibrils, and therefore those involving αC domain interactions, break before the complete rupture of the protofibrils.

Fibrin fibers show irreversible damage under load

LFM mechanical testing shows that fibrin fibers exhibit a behavior under cyclic loading that is not purely viscoelastic, exhibiting a different behavior from the initial loading—a phenomenon known as "preconditioning" observed in various biological materials.[21,60,61] This behavior shares similarities

with Mullin's effect, a phenomenon extensively studied in rubber-like materials.[41] In a pure Mullin's effect, the subsequent loading follows the previous unloading path, indicating altered material properties due to permanent damage.[62] While a pure Mullin's effect entails irreversible damage, which leads to different loading/unloading paths, viscoelastic materials dissipate some energy, leading to a more substantial decay in the unloading curve. Although the damage from the Mullin's effect is largely irrecoverable, materials can recover some energy loss due to viscoelasticity. For a pure viscoelastic material, the second loading would follow the first loading with a Lissajous loop observable during unloading. The recovery time after each cycle is also important. Many materials eventually return to their initial state; however, this process is often a very slow process. For instance, Gedalia et al. observed that the lumbar spine did not fully recover even after a recovery period twice the duration of the loading phase.[63] In fibrin fibers, we find the new loading deviates from both the prior loading and unloading paths, instead following a new trajectory between these curves, a result of a combined Mullin's-like effect and viscoelasticity (Fig. 2C and G), similar to the mechanical behavior observed in electrospun poly(ε-caprolactone) single fibers.[64]

In small strains, fibrin fibers primarily exhibit viscoelastic behavior, where the first and second loadings coincide. This trend persists up to larger strains (∼20%) in partially cross-linked fibers, after which permanent damage is seen; however, uncross-linked fibers start showing permanent damage at ∼15% strain. Cross-linking and covalent bond formation delay structural damage in fibrin fibers up to larger strains. Cyclic loading experiments on bulk fibrin gels also demonstrated the same mechanical irreversibility.[31,65] Kurniawan et al., suggested that network remodeling and the formation of new bonds between fibers may be one mechanism underlying mechanical adaptation in fibrin gels at the macro scales.[31]

Fibrin's unfolding pattern depends on its loading history

The BCARS results complement the LFM mechanical data, providing insights into the molecular structural alterations occurring within fibrin fibers. Due to the non-affine nature of fibrin networks,[66] we avoid directly attributing the macroscopic strain measured in BCARS experiments to the strain experienced by individual fibers or molecules in other experiments. Instead, we use each experimental approach to provide complementary insights, which together contribute to a more comprehensive mechanistic understanding.

To study the secondary structure of fibrin, we focused on the α-helix to β-sheet ratio. Proteins exhibit a key vibrational band in the Amide I region (1600–1700 cm^{-1}), primarily arising from C=O stretching in the peptide backbone. The exact position of the Amide I peak is sensitive to the protein's secondary structure due to changes in the hydrogen bonding environment; for example, α-helices typically produce a peak between 1645–1655 cm^{-1}, while β-sheets appear between 1669–1679 cm^{-1}.[35] By calculating the ratio of mean intensities of the α-helix to β-sheet, we can assess changes in fibrin's secondary structure under mechanical load, focusing on these two dominant motifs. This metric allows

evaluation of structural changes such as unfolding, motif transitions, and their potential reversibility, as demonstrated in previous studies.[25,26]

In uncross-linked fibers, a significant increase in the α-helix to β-sheet ratio is observed under a small strain of 16%, a phenomenon notably absent in partially cross-linked fibers where the ratio remains relatively stable throughout the first and second loadings. This significant unfolding apparently results in more permanent changes in fibrin's secondary structure as the ratio does not return to the original value that it was in the initial state. This signifies only partial refolding of the chains, even in response to small strains.

The unexpected increase in the α-helix to β-sheet ratio during cyclic loadings in uncross-linked fibers contrasts with the typically observed transition towards a decreasing ratio under load.[25,26] This may be explained by MD simulations for uncross-linked fibrinogen molecule showing that both α-helices and β-sheets unfold under the applied force in both γ-nodule and coiled-coil structures. While some α-helices are able to recover back to their previous state, β-sheets show minimal recovery. Even larger β-sheets, such as Gly188–Arg197, which are located away from the pulling point (ILE394), undergo unfolding. This suggests that β-sheets are more susceptible to damage compared to α-helices at least at low strains. Interestingly, in the coiled-coil regions, loops play a crucial role in the folding and unfolding dynamics of the entire structure. The loss of loops during the initial pulling phase may also explain the increased α-helix/β-sheet ratio. In previous studies, Litvonov *et al.*, Fleissner *et al.*, and Wang *et al.*, all observed that the ratio decreases in higher strains for cross-linked and partially cross-linked fibers, respectively.[25,26,67] At lower strains, this decrease was detected in regions adjacent to gel cracks, where local stresses are elevated.[68] In our case, we only observed that the ratio increases for uncross-linked fibers and at low strain of 16.66%. Partially cross-linked fibers did not show significant changes even at 66% (Fig. 3E). The sawtooth pattern of force–extension curves from AFM single molecule force spectroscopy is another indication of β-sheet unfolding.[44] Our MD simulations were consistent with the previous works, showing unfolding in the γ-nodule and coiled-coil structures and also confirmed our experimental results for uncross-linked fibers. Additionally, we observed the decreasing pattern of α-helix to β-sheet ratio in our control experiment under acyclic, unidirectional (always increasing) tensile deformation in partially cross-linked fibrin gels (Fig. S14C), consistent with the previous studies above.[25,26,67] Overall, the unfolding/refolding behavior of fibrinogen appears to be a complex, mixed phenomenon involving multiple domains. This complexity is also supported by AFM force spectroscopy and MD simulations of double-stranded fibrin oligomers under load which demonstrate simultaneous unfolding transitions across different domains.[27]

Conversely, in partially cross-linked fibers, Raman spectroscopy showed no significant difference among various states, which exhibit less force propagation to the fibrin molecules and, hence, fewer changes in their secondary structure under small or even large strains (up to 66%). This is consistent with mechanical results of partially cross-linked fibers where less

damage is observed in small strains. Also, cross-linked fibrin fibers show permanent damage in larger strains compared to uncross-linked fibers,[19] meaning cross-linking reduces the applied force to the fibrin molecules and, hence, significant molecular changes. Additionally, the α-helix to β-sheet ratio differs in two consecutive loadings with the same amount of strain. In uncross-linked fibers, compared to the first pull, the ratio is larger in the second pull, but in partially cross-linked fibers, it becomes smaller. We attribute this difference to the damage that is applied to different domains in the fibrin molecule. The stiffness in protein's different domains changes upon the first loading, which causes a redistribution of deformation and hence a different mechanical response in the second loading (with the same amount of strain). A similar analysis could be applied to mutated fibrinogen molecules,[69] which may result in distinct fibrin gels. For example, the BβArg448Lys and AαArg554Cys variants produce thinner fibers with smaller pores, resulting in stiffer gels,[70,71] whereas the γAla353Ser and γArg275Cys mutations lead to thicker fibers compared to the control.[72,73] Interestingly, even mutations at the same residue can yield different clotting behaviors: the γAsp364Ala and γAsp364His mutations have been reported to produce distinct outcomes, with the latter completely preventing fibrin gel formation.[74] Together, these observations underscore the complex and heterogeneous nature of the fibrinogen molecule, making it difficult to predict its behavior based solely on mutation location or type.

3D conformation of fibrin changes under load

Aromatic amino acids, mainly present in the D-domain of the fibrinogen molecule (depicted in Table S3), exhibit hydrophobic properties with a distinct peak at ∼3065 cm^{-1} (ref. 36 and 75) and play a role in the tertiary (3D) conformation of fibrin. This has led to a decrease in the Raman intensity at 3065 cm^{-1}, illustrated in large strains in Fig. 3C and E. While this pattern is observed in uncross-linked fibrin fibers, partially cross-linked fibers exhibit this behavior only in large strains. We attribute this difference to the effect of cross-linking that limits force propagation through fibrin's molecule until large strains are reached.

Additionally, aromatic amino acid intensity demonstrates significant irreversible changes in large strains for uncross-linked fibers, highlighting 3D conformational changes in the tertiary structure of the protein, likely coming from the D-domain as it has the largest portion of aromatic amino acids (Table S3). However, more reversibility is observed for the same level of strain in cross-linked fibers, consistent with mechanical testing results.

While our study aimed to elucidate the molecular nature and mechanism of damage propagation in fibrin, it has certain limitations. The LFM single-fiber pulling technique, although widely used for single-fiber studies,[9,54] is susceptible to several sources of error, including lateral calibration inaccuracies, uncertainty in the vertical position of the tip relative to the fiber, and potential slippage of fibers over the ridges. In our mechanical simulations, we modeled single fibrin fibers as incompressible materials. Although fibrin gels exhibit measurable volume changes

under load,[76] to our knowledge, the volume change of individual fibrin fibers has never been quantified. Without accurate measurements of how a single fiber's volume changes during loading, we could not precisely account for the stresses arising from such changes.

Our MD simulations also relied on simplified structural assumptions, and the crystal structure used lacks the C-terminal regions of all three chains, as well as most of the highly flexible and intrinsically disordered αC domain of the Aα chain. We note that the αC domain has not shown a substantial impact in single-molecule force spectroscopy[44] and can be neglected for single molecule simulations, but it contributes significantly at the fiber and network scales.[19] Consequently, our simulations did not capture precisely how forces are transmitted through this domain and instead focused solely on force propagation *via* knob–hole interactions. We sought to partially address this limitation through our BCARS analysis of fibrin gels under small strains, where the αC domain is primarily involved.

Conclusion

Fibrin fibers, with their hierarchical structure and mechanical properties, are integral to the clotting process. Their behavior under dynamic forces diverges from their response to static loading, highlighting the complexity of their mechanical response. Permanent changes in secondary structure and 3D conformation, influenced by loading history, significantly impact fibrin's mechanical behavior. This understanding enriches our insight into clot behavior under dynamic blood flow pressure or muscle contractions, offering valuable perspectives for understanding the physiological processes and potential therapeutic interventions in clot-related pathologies.

Author contributions

S. N. and S. H. P. conceived the study. S. N. performed all experiments in the study with help from C. M. J. and D. W. M. J. L. and M. K. R. performed the modeling of cyclic loading and damage at the fiber level. M. M. and P. R. performed the molecular dynamics simulations of fibrin protein structure under cyclic loading. S. N. and S. H. P. wrote the manuscript with input from all authors. S. H. P. supervised the study.

Conflicts of interest

M. K. R. has a speaking agreement with Edwards Lifesciences. The remaining authors declare no competing interests.

Data availability

All data for each main text figure in this article are available at the UT Austin Box repository *via* the following link: **https://utexas.box.com/v/FibrinLoadingDamageData**.

Supplementary information (SI) contains supporting figures is also available. See DOI: **https://doi.org/10.1039/d5sm00681c**.

References

1 S. T. Lord, Fibrinogen and fibrin: scaffold proteins in hemostasis, *Curr. Opin. Hematol.*, 2007, **14**, 236.

2 A. S. Wolberg, Thrombin generation and fibrin clot structure, *Blood Rev.*, 2007, **21**, 131–142.

3 J. W. Weisel, Fibrinogen and Fibrin, *Advances in Protein Chemistry*, Academic Press, 2005, vol. 70, pp. 247–299.

4 M. W. Mosesson, Fibrinogen and fibrin structure and functions, *J. Thromb. Haemostasis*, 2005, **3**, 1894–1904.

5 J. W. Weisel and L. Medved, The Structure and Function of the αC Domains of Fibrinogen, *Ann. N. Y. Acad. Sci.*, 2001, **936**, 312–327.

6 L. V. Medved', O. V. Gorkun, V. F. Manyakov and V. A. Belitser, The role of fibrinogen alpha C-domains in the fibrin assembly process, *FEBS Lett.*, 1985, **181**, 109–112.

7 L. Lorand, Factor XIII: Structure, Activation, and Interactions with Fibrinogen and Fibrin, *Ann. N. Y. Acad. Sci.*, 2001, **936**, 291–311.

8 T. Feller, S. D. A. Connell and R. A. S. Ariens, Why fibrin biomechanical properties matter for hemostasis and thrombosis, *J. Thromb. Haemostasis*, 2022, **20**, 6–16.

9 W. Liu, C. R. Carlisle, E. A. Sparks and M. Guthold, The mechanical properties of single fibrin fibers, *J. Thromb. Haemostasis*, 2010, **8**, 1030–1036.

10 I. K. Piechocka, R. G. Bacabac, M. Potters, F. C. MacKintosh and G. H. Koenderink, Structural Hierarchy Governs Fibrin Gel Mechanics, *Biophys. J.*, 2010, **98**, 2281–2289.

11 R. W. Rosser, W. W. Roberts and J. D. Ferry, Rheology of fibrin clots: IV. Darcy constants and fiber thickness, *Biophys. Chem.*, 1977, **7**, 153–157.

12 C. Gerth, W. W. Roberts and J. D. Ferry, Rheology of fibrin clots II: Linear viscoelastic behavior in shear creep, *Biophys. Chem.*, 1974, **2**, 208–217.

13 J. W. Weisel, The mechanical properties of fibrin for basic scientists and clinicians, *Biophys. Chem.*, 2004, **112**, 267–276.

14 G. P. Sugerman, S. H. Parekh and M. K. Rausch, Nonlinear, dissipative phenomena in whole blood clot mechanics, *Soft Matter*, 2020, **16**, 9908–9916.

15 Y.-U. Lee, A. Y. Lee, J. D. Humphrey and M. K. Rausch, Histological and biomechanical changes in a mouse model of venous thrombus remodeling, *Biorheology*, 2015, **52**, 235–245.

16 E. X. Brown André, R. I. Litvinov, D. E. Discher and J. W. Weisel, Forced Unfolding of Coiled-Coils in Fibrinogen by Single-Molecule AFM, *Biophys. J.*, 2007, **92**, L39–L41.

17 A. Zhmurov, *et al.*, Mechanism of Fibrin(ogen) Forced Unfolding, *Structure*, 2011, **19**, 1615–1624.

18 J.-P. Collet, *et al.*, The αC domains of fibrinogen affect the structure of the fibrin clot, its physical properties, and its susceptibility to fibrinolysis, *Blood*, 2005, **106**, 3824–3830.

19 C. C. Helms, R. A. S. Ariëns, S. Uitte de Willige, K. F. Standeven and M. Guthold, α–α Cross-Links Increase Fibrin Fiber Elasticity and Stiffness, *Biophys. J.*, 2012, **102**, 168–175.

20 S. Münster, *et al.*, Strain history dependence of the non-linear stress response of fibrin and collagen networks, *Proc. Natl. Acad. Sci. U. S. A.*, 2013, **110**, 12197–12202.

21 J. L. Emery, J. H. Omens and A. D. McCulloch, Strain Softening in Rat Left Ventricular Myocardium, *J. Biomech. Eng.*, 1997, **119**, 6–12.

22 L. Schatzmann, P. Brunner and H. U. Stäubli, Effect of cyclic preconditioning on the tensile properties of human quadriceps tendons and patellar ligaments, *Knee Surg. Sports Traumatol. Arthrosc.*, 1998, **6**, S56–S61.

23 J.-P. Collet, H. Shuman, R. E. Ledger, S. Lee and J. W. Weisel, The elasticity of an individual fibrin fiber in a clot, *Proc. Natl. Acad. Sci. U. S. A.*, 2005, **102**, 9133–9137.

24 F. Fleissner, M. Bonn and S. H. Parekh, Microscale spatial heterogeneity of protein structural transitions in fibrin matrices, *Sci. Adv.*, 2016, **2**, e1501778.

25 R. I. Litvinov, D. A. Faizullin, Y. F. Zuev and J. W. Weisel, The α-Helix to β-Sheet Transition in Stretched and Compressed Hydrated Fibrin Clots, *Biophys. J.*, 2012, **103**, 1020–1027.

26 Y. Wang, *et al.*, Probing fibrin's molecular response to shear and tensile deformation with coherent Raman microscopy, *Acta Biomater.*, 2021, **121**, 383–392.

27 F. Maksudov, *et al.*, Structural Mechanisms of Forced Unfolding of Double-Stranded Fibrin Oligomers, *J. Phys. Chem. B*, 2025, **129**, 3963–3977.

28 S. H. Parekh, O. Chaudhuri, J. A. Theriot and D. A. Fletcher, Loading history determines the velocity of actin-network growth, *Nat. Cell Biol.*, 2005, **7**, 1219–1223.

29 D. Krajcinovic, *Damage Mechanics*, Elsevier, 1996.

30 W. Liu, *et al.*, Fibrin Fibers Have Extraordinary Extensibility and Elasticity, *Science*, 2006, **313**, 634.

31 N. A. Kurniawan, *et al.*, Fibrin Networks Support Recurring Mechanical Loads by Adapting their Structure across Multiple Scales, *Biophys. J.*, 2016, **111**, 1026–1034.

32 H. A. Belcher, M. Guthold and N. E. Hudson, What is the diameter of a fibrin fiber?, *Res. Pract. Thromb. Haemostasis*, 2023, **7**, 100285.

33 Y. Gidi, S. Bayram, C. J. Ablenas, A. S. Blum and G. Cosa, Efficient One-Step PEG-Silane Passivation of Glass Surfaces for Single-Molecule Fluorescence Studies, *ACS Appl. Mater. Interfaces*, 2018, **10**, 39505–39511.

34 J. M. Sharpe, H. Lee, A. R. Hall, K. Bonin and M. Guthold, Mechanical Properties of Electrospun, Blended Fibrinogen: PCL Nanofibers, *Nanomaterials*, 2020, **10**, 1843.

35 Z. Movasaghi, S. Rehman and I. U. Rehman, Raman Spectroscopy of Biological Tissues, *Appl. Spectrosc. Rev.*, 2007, **42**, 493–541.

36 N. K. Howell, G. Arteaga, S. Nakai and E. C. Y. Li-Chan, Raman Spectral Analysis in the C–H Stretching Region of Proteins and Amino Acids for Investigation of Hydrophobic Interactions, *J. Agric. Food Chem.*, 1999, **47**, 924–933.

37 Violin Plot, 2024, **https://www.mathworks.com/matlabcentral/fileexchange/45134-violin-plot**.

38 H. A. Belcher, M. Guthold and N. E. Hudson, What is the diameter of a fibrin fiber?, *Res. Pract. Thromb. Haemostasis*, 2023, **7**, 100285.

39 J. C. Simo and T. J. R. Hughes, *Computational Inelasticity*, Springer Science & Business Media, 2006.

40 J. C. Simo, On a fully three-dimensional finite-strain viscoelastic damage model: Formulation and computational aspects, *Comput. Methods Appl. Mech. Eng.*, 1987, **60**, 153–173.

41 L. Mullins, Softening of Rubber by Deformation, *Rubber Chem. Technol.*, 1969, **42**, 339–362.

42 R. F. Doolittle, K. W. K. Watt, B. A. Cottrell, D. D. Strong and M. Riley, The amino acid sequence of the α-chain of human fibrinogen, *Nature*, 1979, **280**, 464–468.

43 J. M. Kollman, L. Pandi, M. R. Sawaya, M. Riley and R. F. Doolittle, Crystal Structure of Human Fibrinogen, *Biochemistry*, 2009, **48**, 3877–3886.

44 A. Zhmurov, *et al.*, Mechanism of Fibrin(ogen) Forced Unfolding, *Structure*, 2011, **19**, 1615–1624.

45 D. Van Der Spoel, *et al.*, GROMACS: Fast, flexible, and free, *J. Comput. Chem.*, 2005, **26**, 1701–1718.

46 M. J. Abraham, *et al.*, GROMACS: High performance molecular simulations through multi-level parallelism from laptops to supercomputers, *SoftwareX*, 2015, **1–2**, 19–25.

47 P. Bjelkmar, P. Larsson, M. A. Cuendet, B. Hess and E. Lindahl, Implementation of the CHARMM Force Field in GROMACS: Analysis of Protein Stability Effects from Correction Maps, Virtual Interaction Sites, and Water Models, *J. Chem. Theory Comput.*, 2010, **6**, 459–466.

48 P. Eastman, *et al.*, OpenMM 8: Molecular Dynamics Simulation with Machine Learning Potentials, *J. Phys. Chem. B*, 2024, **128**, 109–116.

49 N. Michaud-Agrawal, E. J. Denning, T. B. Woolf and O. Beckstein, MDAnalysis: A toolkit for the analysis of molecular dynamics simulations, *J. Comput. Chem.*, 2011, **32**, 2319–2327.

50 R. J. Gowers, *et al.*, MDAnalysis: A Python Package for the Rapid Analysis of Molecular Dynamics Simulations, *Scipy*, 2016, 98–105, DOI: **10.25080/Majora-629e541a-00e**.

51 F. Carrascoza, S. Zaric and R. Silaghi-Dumitrescu, Computational study of protein secondary structure elements: Ramachandran plots revisited, *J. Mol. Graphics Modell.*, 2014, **50**, 125–133.

52 S. A. Hollingsworth and P. A. Karplus, A fresh look at the Ramachandran plot and the occurrence of standard structures in proteins, *Biomol. Concepts*, 2010, **1**, 271–283.

53 W. Li, *et al.*, Nonuniform Internal Structure of Fibrin Fibers: Protein Density and Bond Density Strongly Decrease with Increasing Diameter, *BioMed Res. Int.*, 2017, **2017**, e6385628.

54 F. Maksudov, *et al.*, Strength, deformability and toughness of uncrosslinked fibrin fibers from theoretical reconstruction of stress-strain curves, *Acta Biomater.*, 2021, **136**, 327–342.

55 A. R. Wufsus, *et al.*, Elastic Behavior and Platelet Retraction in Low- and High-Density Fibrin Gels, *Biophys. J.*, 2015, **108**, 173–183.

56 M. Berjot, J. Marx and A. J. P. Alix, Determination of the secondary structure of proteins from the Raman amide I band: The reference intensity profiles method, *J. Raman Spectrosc.*, 1987, **18**, 289–300.

57 J. W. Weisel and R. I. Litvinov, Fibrin Formation, Structure and Properties, in *Fibrous Proteins: Structures and Mechanisms*, ed. D. A. D. Parry and J. M. Squire, Springer International Publishing, Cham, 2017, pp. 405–456, DOI: **10.1007/978-3-319-49674-0_13**.

58 H. F. Brinson and L. C. Brinson, *Polymer Engineering Science and Viscoelasticity*, Springer US, Boston, MA, 2008, DOI: **10.1007/978-0-387-73861-1**.

59 M. T. Shaw and W. J. MacKnight, Transitions and Relaxation in Amorphous Polymers, in *Introduction to Polymer Viscoelasticity*, ed. M. T. Shaw and W. J. MacKnight, 2005.

60 Y. C. Fung, *Biomechanics: Mechanical Properties of Living Tissues*, Springer Science & Business Media, 2013.

61 K. S. Miller, L. Edelstein, B. K. Connizzo and L. J. Soslowsky, Effect of Preconditioning and Stress Relaxation on Local Collagen Fiber Re-Alignment: Inhomogeneous Properties of Rat Supraspinatus Tendon, *J. Biomech. Eng.*, 2012, **134**(3), 031007.

62 K. M. Schmoller and A. R. Bausch, Similar nonlinear mechanical responses in hard and soft materials, *Nat. Mater.*, 2013, **12**, 278–281.

63 U. Gedalia, *et al.*, Biomechanics of Increased Exposure to Lumbar Injury Caused by Cyclic Loading: Part 2. Recovery of Reflexive Muscular Stability With Rest, *Spine*, 1999, **24**, 2461.

64 D. Alexeev, N. Goedecke, J. Snedeker and S. Ferguson, Mechanical evaluation of electrospun poly(ε-caprolactone) single fibers, *Mater. Today Commun.*, 2020, **24**, 101211.

65 S. Liu, A. Bahmani, F. Ghezelbash and J. Li, Fibrin clot fracture under cyclic fatigue and variable rate loading, *Acta Biomater.*, 2024, **177**, 265–277.

66 Q. Wen, A. Basu, A. Janmey P. and G. Yodh A., Non-affine deformations in polymer hydrogels, *Soft Matter*, 2012, **8**, 8039–8049.

67 F. Fleissner, M. Bonn and S. H. Parekh, Microscale spatial heterogeneity of protein structural transitions in fibrin matrices, *Sci. Adv.*, 2016, **2**, e1501778.

68 D. Liu, *et al.*, Molecular Creep Induced Fatigue Rupture of Fibrin Clots, *Adv. Sci.*, 2025, e05109.

69 R. Asselta, S. Duga and M. L. Tenchini, The molecular basis of quantitative fibrinogen disorders, *J. Thromb. Haemostasis*, 2006, **4**, 2115–2129.

70 R. Ajjan, *et al.*, Common variation in the C-terminal region of the fibrinogen β-chain: effects on fibrin structure, fibrinolysis and clot rigidity, *Blood*, 2008, **111**, 643–650.

71 J. Collet, *et al.*, Dusart syndrome: a new concept of the relationship between fibrin clot architecture and fibrin clot degradability: hypofibrinolysis related to an abnormal clot structure, *Blood*, 1993, **82**, 2462–2469.

72 R. Marchi, *et al.*, Fibrin clot properties to assess the bleeding phenotype in unrelated patients with hypodysfibrinogenemia due to novel fibrinogen mutations, *Thromb. Res.*, 2021, **197**, 56–64.

73 S. Ishikawa, *et al.*, Recombinant fibrinogen, γ275Arg → Cys, exhibits formation of disulfide bond with cysteine and severely impaired D:D interactions, *J. Thromb. Haemostasis*, 2004, **2**, 468–475.

74 N. Okumura, O. V. Gorkun and S. T. Lord, Severely Impaired Polymerization of Recombinant Fibrinogen γ-364 Asp → His, the Substitution Discovered in a Heterozygous Individual, *J. Biol. Chem.*, 1997, **272**, 29596–29601.

75 A. M. Kinney and G. Eleazar, *Assessment of protein surface hydrophobicity by spectroscopic methods and its relation to emulsifying properties of proteins*, University of British Columbia, 1994, DOI: **10.14288/1.0088026**.

76 J. M. Jimenez, *et al.*, Multiscale mechanical characterization and computational modeling of fibrin gels, *Acta Biomater.*, 2023, **162**, 292–303.